symmetry

MDPI

Article

Nonlinear Receding Contact Mechanics of Functionally Graded Layers for Aerospace Structures: A Symmetry-Based Analytical and FEM Study

Ahmad Abushattal [1,2,*], Merve Terzi [3], Ayşegül Eyüboğlu [4], Murat Yaylacı [3,5,*], Dursun Murat Sekban [6], Safa Nayır [4], Ecren Uzun Yaylacı [7], Deshinta Arrova Dewi [8] and Ahmet Birinci [4]

1 Centro Singular de Investigación en Tecnoloxías de Información (CiTIUS), Universidad de Santiago de Compostela, 15705 Santiago de Compostela, Spain
2 Department of Physics, Al-Hussein Bin Talal University, Ma'an 71111, Jordan
3 Department of Civil Engineering, Recep Tayyip Erdogan University, Rize 53100, Türkiye; merveterzii94@gmail.com
4 Department of Civil Engineering, Karadeniz Technical University, Trabzon 61080, Türkiye; aysegul_eyuboglu@hotmail.com (A.E.); safanayir@ktu.edu.tr (S.N.); birinci@ktu.edu.tr (A.B.)
5 Turgut Kıran Maritime Faculty, Recep Tayyip Erdogan University, Rize 53900, Türkiye
6 Department of Marine Engineering Operations, Karadeniz Technical University, Trabzon 61530, Türkiye; msekban@ktu.edu.tr
7 Faculty of Fisheries, Recep Tayyip Erdogan University, Rize 53100, Türkiye; ecren.uzunyaylaci@erdogan.edu.tr
8 Faculty of Data Science and Information Technology, INTI International University, Nilai 1800, Negeri Sembilan, Malaysia; deshinta.ad@newinti.edu.my
* Correspondence: ahmad.abushattal@usc.es (A.A.); murat.yaylaci@erdogan.edu.tr (M.Y.)

Abstract

Functionally graded materials (FGMs) are widely applied in spacecraft structural design, thermal protection systems, and planetary landing mechanisms, benefiting from their ability to resist large thermal, pressure, and force gradients. To assess structural response behaviors for lander missions, docking maneuvers, and force transfer in layered aerospace structures, analyzing the contacts subjected to heavily stressed areas becomes very important. This article investigates the receding contact between a functionally graded top layer and a uniform substrate lying on a Winkler elastic foundation using the elasticity theory. An analytical approach has been validated using a finite element method (FEM) implemented in ANSYS. Comparison between the analytical solution and the FEM solution has been conducted for different stamp radii, elastic foundation stiffnesses, and ratios of shearing modulus for various realistic materials in the aerospace field. The data indicate very good convergence between the two solutions for both the length of contacts and the normal stress distribution, where differences are always below 3%. An increase in stamp radius leads to an extension of the contacts as well as a reduction in normal stresses and elevated stiffness and shearing modulus ratio contribute to smaller contacts and higher stresses. The validated methodological approach offers a realistic means for predicting force transfer mechanisms in spacecraft landing pads, multi-layer insulation panels, adaptive space structures, and functionally graded parts subjected to localized loads. This work offers predictive capabilities for space material interface design and optimization for harsh mechanical environments.

Keywords: functionally graded materials; receding contact mechanics; finite element method; process innovation; aerospace structures

Check for updates

Academic Editors: Olexiy Shynkarenko, Antonella Ingenito and Maksym Ziberov

Received: 23 January 2026
Revised: 8 February 2026
Accepted: 13 February 2026
Published: 19 February 2026

Copyright: © 2026 by the authors. Licensee MDPI, Basel, Switzerland. This article is an open access article distributed under the terms and conditions of the Creative Commons Attribution (CC BY) license.

1. Introduction

Elastic-layer interaction problems with either point or distributed loads are typical in space launching design concepts [1,2]. Conditions encountered during landing maneuvers on other planets, deployment of rovers on planetary bodies, docking operations between space vehicles, and between space vehicles and their structural parts involve elastic layers that suffer local loads to which stress transfer and structural integrity are sensitive. Specifically, where landers touch planetary surfaces with layers of fine regolitic material resting on top of compacted layers, interfacial recession or expansion areas are important for stability and safe touchdowns [3,4]. Also, space vehicles' thermal protection layers, structural panels, and compositional layer materials are often subjected to severe mechanical and thermomechanical environments where stress transfer between interfacial layers becomes essential [5–7]. The need for FGMs has also intensified in spacecraft design missions with extreme variations in environmental factors. Their ability to change properties continually to reduce interfacial stress, enhance thermal shock resistance, or optimize elastic properties for space missions qualifies them for various applications in spacecraft design missions [8,9]. Some applications include heat-protection subsystems, spacecraft insulation panels, propulsion parts, and layers for suppressing vibrations in satellite structures. In particular, graded landing pad interfaces, thermal protection system layers, and multi-layer structural panels in spacecraft frequently experience evolving contact conditions where stress redistribution is strongly influenced by material gradation. It is also important to understand how FGMs react when they are in contact with other layers or elements [10–13].

Contact problems with receding contacts, where the size of the contact region varies with respect to the applied loads, form a complex but realistic problem that can be encountered in space missions. During landing on stratified regolths or when using end-effectors on stratified spacecraft materials, the size of the actual contact region varies according to material gradations, elasticity contrasts, and geometric scaling. This nonlinear problem, very sensitive to the parameters, requires advanced mathematical models to correctly capture boundaries and stress transmissions for strongly contrasting material properties. Although contact behavior in graded materials has been examined in the literature, many existing studies assume fixed contact regions or homogeneous layer configurations, which limits their applicability to evolving the graded-layer systems encountered in aerospace applications [14–18]. In our research, we focus on a two-layer contact problem, where one layer is functionally graded while the other is homogeneous, placed on top of an elastic foundation [19]. The problem can be described using elasticity theory and has been analyzed using finite element simulations within the ANSYS environment to calculate the resulting data on contact length and normal stresses for various cases of loadings and material properties. Although our problem has a general nature, to give credit to its engineering applications we chose parameter values reflecting certain examples of material pairs applied in spacecraft design, landing accessories, and other space engineering tasks [20,21].

A contact problem describes the behavior of surfaces or elements that come into contact with each other. All these aspects involve the intricate nature of solid materials meeting at points of contact [22,23]. Various researchers have scrutinized the effects of different forces, especially pressure, on these materials. This kind of study is not only theoretical; it forms the backbone of material behavior during operation. Contact areas moving away due to forces form a problem that sets out to look at the receding contact problem [23,24]. This problem assumes significance with respect to material behavior during dynamic operation when the contact area at the commencement of operation needs due attention but may reduce or recede due to different forces and factors. FGMs encompass different properties that suit different applications. Applying FGM technology may allow us to come up

with special solutions regarding different contact problems, including the receding contact problem [10,25].

To counter the property gradients of the contact problem, specific analytical techniques, and the FEM, are required to cope with the property gradients of the FGMs [26,27]. Analytical techniques are based on mathematical equations and theories that are used to solve a problem without relying on simulations and approximations. This particular theory finds its application area within the study of elasticity. The study of elasticity deals with the study of the behavior of solid materials under the action of force and their resulting material characteristics of deformation and stress. The material should revert back to its original form after the force action ceases; this phenomenon of reverting back to the original form after the force ceases to act is called elasticity [24,28]. This theory of elasticity assists in the measurement of the prediction of the phenomenon of deformation that occurs due to the application of pressure on the different layers of the material with the aid of the cylindrical stamp. One of the layers of the material is an FGM, meaning that the material varies in depth. Application of the principles of elasticity assists in predicting the deformation of the material due to the force of pressure that comes with the application of the cylindrical stamp [29,30]. The deformation of layered materials subjected to pressure from a cylindrical stamp can be predicted on the basis of the elasticity theory. This theory defines how materials change shape when they are subjected to certain loads and how they recover to their original form once the load has ceased to act [30]. For solving this kind of problem, mathematical concepts, for example, Fourier and Laplace transformations, are applied. For instance, using these transformations, the problem regarding deformation can be simplified. As a result, equations can be derived to calculate how the pressure applied by the cylindrical stamp affects each layer of material [31]. This approach enables one to understand how various layers work when subjected to loads and how deformation evolves in the structure. Applying elasticity concepts coupled with transformations can effectively predict how materials will react to a cylindrical stamping action.

An FEM is employed to analyze a frictionless receding contact problem of the type that involves two layers with a layer of FGM, and the results are checked using an analytical approach that depends on the theory of elasticity [32,33]. Apart from flexibility and adaptability, the utility of FEMs extends over a broad area of problems of various disciplines including structural analysis and fluid mechanics. The software employed here is ANSYS R1 (25.1). This software depends on a FEM as its mathematical base for the decomposition, solution of problems, and subsequent analysis of complicated theories [34]. Aspects of flexibility of ANSYS lie in the application of FEMs over a broad area of different subjects that encompass the analysis of structures, heat transfer analysis, hydrodynamics analysis, and electricity [35,36]. A frictionless receding contact problem will be studied here. An upper layer of FGM material with a homogeneous lower layer on the Winkler foundation will be studied. It examines the transmission of compressive normal tractions between these components under frictionless contact. The deformation and stress of materials can be understood using traditional analytical methods, which employ elasticity theory. Further, FEM simulations using ANSYS software allow the granular analysis of FGM layers of varying properties. This paper compares the precision of the analytical method and the flexibility of the FEM [36,37]. Comparative methodologies not only validate these approaches but also provide valuable insights for future research and practical applications.

The present work addresses the basic mechanics and symmetry properties of receding contact in layered systems and provides a validated analytical–numerical solution that is generic to aerospace structures rather than representing a particular mission configuration. In contrast to existing studies that focus primarily on either analytical formulations or numerical simulations, this study establishes a symmetry-based analytical model for a

layered system composed of an exponentially graded FGM layer and a homogeneous substrate on a Winkler foundation, and validates it through FEM analysis. The originality of the work lies in the simultaneous analysis of both the stamp FGM and FGM substrate contact interfaces under varying geometric, stiffness, and material gradation parameters within a single consistent analytical and numerical framework.

2. Analytical Solution

The analytical solution concerns an FG layer in contact with an elastic homogeneous layer on a Winkler foundation under a rigid cylindrical stamp, given in Figure 1 below. Since there is no friction in the contacts at the interfaces, there are only normal compression forces acting on the interfaces. This assumption is commonly adopted in contact mechanics to isolate normal stress transfer mechanisms and to obtain closed-form analytical solutions. In many aerospace and layered structural applications, contact surfaces may experience limited tangential interaction due to lubrication effects, compliant coatings, or dominant normal loading conditions, making this approximation a reasonable first-order idealization. Gravity is not considered in these systems. This assumption is reasonable because the analysis focuses on localized contact stresses induced by the applied stamp load, which are significantly larger than the distributed body forces associated with gravity, particularly in spacecraft landing and structural interface problems where concentrated contact forces dominate the response. In these systems, there is a rigid circular stamp with radius 'R'. It exerts an external concentrated load on the FG layers with a thickness 'h1'. These FG layers with thickness 'h2' are on Winkler foundations with an elastic factor 'k'. The Winkler foundation model idealizes the supporting medium as a set of independent linear springs, where the reaction at each point is proportional to the local displacement. This model is appropriate for layered or compliant supporting media where shear interaction within the foundation is negligible; however, it does not account for continuous shear coupling effects, which represents a known limitation of the Winkler assumption. On these layers with radius 'R', there is a circular stamp in contact with the FG layers in the interval '−a, a'. These FG layers with thickness 'h2' are in contact with homogeneous layers in the interval '−b, b'. These layers have a thickness in the 'z-direction' of unity. The analysis was carried out under plane strain conditions, which is appropriate for long cylindrical contact configurations where deformation in the out-of-plane direction is constrained.

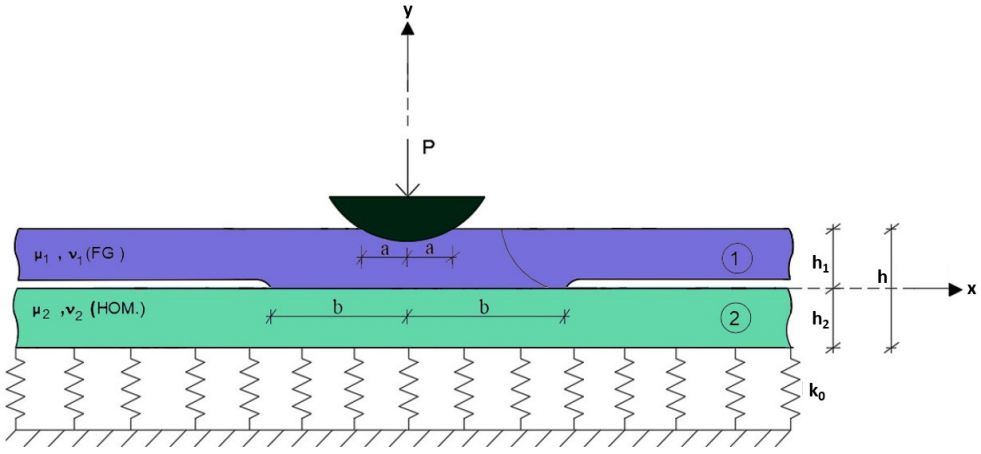


Figure 1. Geometry of the problem: ① FG layer and ② homogeneous layer.

Although the governing elasticity equations are linear within the framework of small deformation theory, the problem exhibits nonlinearity due to the unknown and load-dependent receding contact boundaries (a and b), which render the formulation a nonlinear free-boundary problem. Therefore, the term "nonlinear" in the title refers to the evolving

contact region rather than to geometric or material nonlinearities. The contact regions (a and b) are determined as part of the solution from the mixed boundary conditions and equilibrium equations. The formulation is governed by linear elasticity, small deformation theory, and frictionless contact assumptions.

The graded layer is assumed to be an isotropic medium with properties varying inhomogeneously in the direction of 'y'. ν_1 is the Poisson's ratio which is constant. The shear modulus (μ_1) is an exponential function:

$$\mu_1(y) = \mu_0\, e^{\beta y}\ , \qquad (0\ \leq y\ \leq h_1) \tag{1}$$

where the shear modulus is μ_0 (for y = 0) at the bottom of the FG layer. The stiffness parameter β controls the shear modulus changes in the graded medium. The shear modulus (μ_2) and Poisson's ratio (ν_2) for the homogeneous layer is as follows:

$$\frac{\partial \sigma_{ix}}{\partial x} + \frac{\partial \tau_{ixy}}{\partial y} = 0, \quad \frac{\partial \tau_{iyx}}{\partial x} + \frac{\partial \sigma_{iy}}{\partial y} = 0 \tag{2}$$

$$\sigma_{ix} = \frac{\mu_i}{\kappa_i - 1}\left[(\kappa_i + 1)\frac{\partial u_i}{\partial x} + (3 - \kappa_i)\frac{\partial v_i}{\partial y}\right], \quad (i = 1,\ 2) \tag{3}$$

$$\sigma_{iy} = \frac{\mu_i}{\kappa_i - 1}\left[(3 - \kappa_i)\frac{\partial u_i}{\partial x} + (\kappa_i + 1)\frac{\partial v_i}{\partial y}\right], \quad (i = 1,\ 2) \tag{4}$$

$$\tau_{ixy} = \mu_i\left(\frac{\partial u_i}{\partial y} + \frac{\partial v_i}{\partial x}\right), \quad (i = 1,\ 2) \tag{5}$$

u_i and v_i (i = 1, 2) are the displacement components in the x and y directions shown in Equations (2)–(5); $\kappa_i = 3 - 4\nu_i$ for plane strain and $\kappa_i = (3 - \nu_i)/(1 + \nu_i)$ for plane stress where the Poisson's ratio is ν_i. The stress components are σ_{ix}, σ_{iy} and τ_{ixy}. Also, the shear modulus is denoted by μ_1 for the FG layer and μ_2 for the homogeneous layer. 1 represents the FG layer and 2 represents the homogeneous layer. The two-dimensional elasto-static Navier equations are formed by the combination of Equations (1)–(5). This step is carried out to solve the interactions of the receding contact problem between layer one (FG), and layer two (homogeneous).

$$(\kappa_1 + 1)\frac{\partial^2 u_1}{\partial x^2} + (\kappa_1 - 1)\frac{\partial^2 u_1}{\partial y^2} + 2\frac{\partial^2 v_1}{\partial x \partial y} + \beta(\kappa_1 - 1)\frac{\partial u_1}{\partial y} + \beta(\kappa_1 - 1)\frac{\partial v_1}{\partial x} = 0 \tag{6}$$

$$(\kappa_1 - 1)\frac{\partial^2 v_1}{\partial x^2} + (\kappa_1 + 1)\frac{\partial^2 v_1}{\partial y^2} + 2\frac{\partial^2 u_1}{\partial x \partial y} + \beta(3 - \kappa_1)\frac{\partial u_1}{\partial x} + \beta(\kappa_1 + 1)\frac{\partial v_1}{\partial y} = 0 \tag{7}$$

$$(\kappa_2 + 1)\frac{\partial^2 u_2}{\partial x^2} + (\kappa_2 - 1)\frac{\partial^2 u_2}{\partial y^2} + 2\frac{\partial^2 v_2}{\partial x \partial y} = 0 \tag{8}$$

$$(\kappa_2 - 1)\frac{\partial^2 v_2}{\partial x^2} + (\kappa_2 + 1)\frac{\partial^2 v_2}{\partial y^2} + 2\frac{\partial^2 u_2}{\partial x \partial y} = 0 \tag{9}$$

where x = 0 represents plane symmetry at the point; the problem is solved only in the region $0 \leq x < \infty$. Since the geometry of the cylindrical stamp, the applied load, and the layered configuration are symmetric with respect to the vertical axis (x = 0), the contact problem exhibits geometric and loading symmetry. Therefore, the mathematical formulation is developed only over the half-domain ($x \geq 0$), and appropriate symmetry conditions are imposed to reduce the governing equations and boundary conditions. Taking into account the symmetric property of the problem, the following expressions can be written for

the displacements using the Fourier transform technique—the symmetric property of the problem:

$$u_i(x,y) = \frac{2}{\pi}\int_0^\infty \phi_i(\xi,y)\sin\xi x d\xi, \quad v_i(x,y) = \frac{2}{\pi}\int_0^\infty \psi_i\ (\xi,y)\cos\xi x d\xi \tag{10}$$

where $\phi_i(\xi,y)$ and $\psi_i(\xi,y)$ are the Fourier transforms of $u_i(x,y)$ and $v_i(x,y)$ (i = 1, 2), respectively.

In Equations (6)–(9), partial differential equations are reduced to ordinary differential equations. This part is carried out using Fourier integral transforms. The solutions of these equations are obtained for the FG layer as follows:

$$\phi_1 = \sum_{j=1}^{4} A_j e^{n_j y}, \quad \psi_1 = \sum_{j=1}^{4} A_j m_j e^{n_j y} \tag{11}$$

the properties n_j (j = 1, 2, 3, 4) from these differential equations must be consistent with the equations. Also, the roots of Equation (12) are provided in Appendix B.

$$n^4 + 2\,\beta\, n^3 + (\,\beta^2 - 2\,\xi^2)n^2 - 2\ \xi^2\,\beta\, n + \ \frac{\xi^2\ (3\,\beta^2 + \xi^2 + (\,\xi^2 - \ \beta^2)\,\kappa_1)}{\kappa_1\ +\ 1}\ \ =\ \ 0 \tag{12}$$

Equation (13) is given by the following expression:

$$m_j = \ \frac{(3\ \ \beta + 2\,n_j - \beta\ \ \kappa_1)\ \ [\ \ n_j\ (\ \ \beta + \ \ n_j)\ \ (\kappa_1 + 1) - \xi^2\ \ (\ \ \kappa_1 + 3)]}{\xi[\,4\,\xi^2 - \beta^2(\kappa_1 - 3)\ \ (\kappa_1 + 1)]}\ \ , \quad (j = \ 1,\ \ldots,\ 4) \tag{13}$$

The displacement and stress components for the FG layer were easily obtained as follows:

$$u_1(x,y) = \frac{2}{\pi}\int_0^\infty \sum_{j=1}^{4} A_j e^{n_j y}\sin(\xi x)d\xi, \quad v_1(x,y) = \frac{2}{\pi}\int_0^\infty \sum_{j=1}^{4} A_j m_j e^{n_j y}\cos(\xi x)d\xi \tag{14}$$

$$\sigma_{1x} = \frac{2\mu_0 e^{\beta y}}{\pi(\kappa_1 - 1)}\int_0^\infty \sum_{j=1}^{4} A_j[(3-\kappa_1)m_j n_j + \xi(\kappa_1 + 1)]e^{n_j\ y}\cos(\xi x)d\xi \tag{15}$$

$$\sigma_{1y} = \frac{2\mu_0 e^{\beta y}}{\pi(\kappa_1 - 1)}\int_0^\infty \sum_{j=1}^{4} A_j C_j e^{n_j y}\cos(\xi x)d\xi \tag{16}$$

$$\tau_{1xy} = \frac{2\mu_0 e^{\beta y}}{\pi}\int_0^\infty \sum_{j=1}^{4} A_j D_j e^{n_j y}\sin(\xi x)d\xi \tag{17}$$

The partial differential equations in Equations (6)–(9), for the second homogeneous layer, converted to ordinary differential equations, and their equation is as follows:

$$\frac{d\phi_2{}^4}{d^4 y} - 2\xi^2\frac{d\phi_2{}^2}{d^2 y} + \ \ \xi^4\phi_2 \ \ = \ \ 0 \tag{18}$$

With a solution as follows:

$$\phi_2 = e^{\lambda y} \tag{19}$$

Using Equations (6)–(9), we obtained ϕ_2, ψ_2, and the following expressions for the displacement and stress components were found for the homogeneous layer:

$$u_2(x,y) = \ \ \frac{2}{\pi}\ \ \int_0^\infty \Big[\ (B_1 + B_2 y)e^{-\xi y} + (B_3 + B_4 y)e^{\xi y}\Big]\sin(\xi x)d\xi \tag{20}$$

$$v_2(x,y) = \frac{2}{\pi}\int_0^\infty \left\{ \left[B_1 + \left(\frac{\kappa_2}{\xi} + y \right) B_2 \right] e^{-\xi y} + \left[-B_3 + \left(\frac{\kappa}{\xi} - y \right) B_4 \right] e^{\xi y} \right\} \cos(\xi x) d\xi \tag{21}$$

$$\frac{1}{2\mu_2}\sigma_{2x}(x,y) = \frac{2}{\pi}\int_0^\infty \left\{ \left[\xi(B_1 + B_2 y) - \left(\frac{3-\kappa_2}{2} \right) B_2 \right] e^{-\xi y} + \left[\xi(B_3 + B_4 y) + \left(\frac{3-\kappa_2}{2} \right) B_4 \right] e^{\xi y} \right\} \cos(\xi x) d\xi \tag{22}$$

$$\frac{1}{2\mu_2}\sigma_{2y}(x,y) = \frac{2}{\pi}\int_0^\infty \left\{ -\left[\xi(B_1 + B_2 y) + \left(\frac{1+\kappa_2}{2} \right) B_2 \right] e^{-\xi y} + \left[-\xi(B_3 + B_4 y) + \left(\frac{1+\kappa_2}{2} \right) B_4 \right] e^{\xi y} \right\} \cos(\xi x) d\xi \tag{23}$$

$$\frac{1}{2\mu_2}\tau_{2xy}(x,y) = \frac{2}{\pi}\int_0^\infty \left\{ -\left[\xi(B_1 + B_2 y) + \left(\frac{\kappa_2 - 1}{2} \right) B_2 \right] e^{-\xi y} + \left[\xi(B_3 + B_4 y) - \left(\frac{\kappa_2 - 1}{2} \right) B_4 \right] e^{\xi y} \right\} \sin(\xi x) d\xi \tag{24}$$

In Equations (15)–(18) and (23)–(32), A_j and B_j are unknown functions that arise from the solutions of the differential equations and are determined by the boundary conditions of the problem, while C_j and D_j (j = 1, 2, 3, 4) are known functions.

The plane divergence contact problem needs to be solved subject to the following boundary conditions:

$$\sigma_{1y}(x,h_1) = \left\{ \begin{array}{ccc} -p_1(x) & ; & (0 \le x < a) \\ 0 & ; & (\ a \le x < \infty) \end{array} \right\} \tag{25}$$

$$\tau_{1xy}(x,h_1) = 0, \quad (0 \le x < \infty) \tag{26}$$

$$\sigma_{2y}(x,0) = \left\{ \begin{array}{ccc} -p_2(x) & ; & (0 \le x < b) \\ 0 & ; & (b \le x < \infty) \end{array} \right\} \tag{27}$$

$$\sigma_{1y}(x,0) = \sigma_{2y}(x,0), \quad (0 \le x < \infty) \tag{28}$$

$$\tau_{1xy}(x,0) = 0, \quad (0 \le x < \infty) \tag{29}$$

$$\tau_{2xy}(x,0) = 0, \quad (0 \le x < \infty) \tag{30}$$

$$\sigma_{2y}(x,-h_2) = k_0 \nu_2(x,-h_2), \quad (0 \le x < \infty) \tag{31}$$

$$\tau_{2xy}(x,-h_2) = 0, \quad (0 \le x < \infty) \tag{32}$$

$$\frac{\partial}{\partial x}[v_1(x,h_1)] = \frac{dF(x)}{dx} = f(x), \quad (0 \le x < a) \tag{33}$$

$$\frac{\partial}{\partial x}[\nu_1(x,0) - \nu_2(x,0)] = 0, \quad (0 \le x < b) \tag{34}$$

$$f(x) = \frac{dF}{dx} = \frac{x}{(R^2 - x^2)^{0.5}} \tag{35}$$

The half contact lengths are a and b between the rigid cylindrical stamp/FG layer and the FG/homogeneous layer. $p_1(x)$ and $p_2(x)$ are the primary contact pressures on the contact surfaces, while $F(x)$ describes the profile of the rigid stamp. R denotes the radius of the cylindrical stamp, and k_0 is the elastic spring constant of the Winkler foundation.

The boundary conditions in Equations (25)–(32) allowed us to represent coefficients Aj, Bj in Equations (14)–(17) and (20)–(24) in terms of the prevailing contact pressures $p_1(x)$ and $p_2(x)$. This enabled us to represent the stresses and displacements in Equations (14) and (20) explicitly in terms of these prevailing contact pressures $p_1(x)$ and $p_2(x)$. Now, these unknown prevailing contact pressures $p_1(x)$, and $p_2(x)$ were determined from the mixed boundary conditions in Equations (33) and (34). The boundary conditions in Equations (33) and (34) had not yet been imposed. The boundary condi-

tions in Equations (33) and (34) could be transformed into an integro-equation problem with recourse to some of the transformations, taking into consideration symmetry in the formulation.

$$\frac{2}{\pi}\int_{-a}^{+a} p_1(t_1)\left\{M_1(x_1,t_1)-\frac{\kappa_1+1}{8}\left[\frac{1}{t_1-x_1}\right]\frac{1}{\mu_0 e^{\beta h_1}}\right\}dt_1+\frac{2}{\pi}\int_{-b}^{+b} p_2(t_2)M_2(x_1,t_2)dt_2=\frac{x}{R} \tag{36}$$

$$\frac{2}{\pi}\int_{-a}^{+a} p_1(t_1)N_1(x_2,t_1)dt_1+\frac{2}{\pi}\int_{-b}^{+b} p_2(t_2)\left\{N_2(x_2,t_2)+\frac{\kappa_1+1}{4\mu_1}\left(\frac{1}{t_2-x_2}\right)+L_1(x_2,t_2)\right\}dt_2=0 \tag{37}$$

where Δ_1 and Δ_2 are explained in Appendix A. In addition, k that appears in Equation is defined as follows:

$$k=k_0/\mu_2 \tag{38}$$

The contact pressures $p_1(x)$ and $p_2(x)$ and a and b (the half contact lengths) are unknown in the system of integral equations, i.e., (38). Using equilibrium conditions, a and b were determined by the following equations:

$$\int_{-a}^{a} p_1(t_1)dt=P, \quad \int_{-b}^{b} p_2(t_2)\,dt=P \tag{39}$$

For the above integral equations, dimensionless quantities were used to simplify the numerical analysis:

$$x_1=as_1, \quad x_2=b\,s_2 \tag{40}$$

$$t_1=ar_1, \quad t_2=br_2 \tag{41}$$

$$G_1(r_1)=\frac{h_1}{P}p_1(t_1), \quad G_2(r_2)=\frac{h_1}{P}p_2(t_2) \tag{42}$$

The normalized forms of the integral Equation (38) and the equilibrium Equations (43) and (44) can be expressed as follows:

$$\int_{-1}^{+1} G_1(r_1)\left\{\frac{a}{h_1}M_1(s_1,r_1)-\frac{\kappa_1+1}{8\,e^{\beta h_1}}\left(\frac{1}{r_1-s_1}\right)\right\}dr_1+\frac{b}{h_1}\int_{-1}^{+1} G_2(r_2)M_2(s_1,r_2)dr_2=\frac{\pi}{2}\frac{\mu_0}{P/h_1}\frac{a/h_1}{R/h_1}s_1 \tag{43}$$

$$\frac{a}{h_1}\int_{-1}^{+1} G_1(r_1)N_1(s_2,r_1)dr_1+\int_{-1}^{+1} G_2(r_2)\left[\frac{b}{h_1}N_2(s_2,r_2)+\frac{\kappa_1+1}{8}\left(\frac{1}{r_2-s_2}\right)+\frac{b}{h_1}L_1(s_2,r_2)\right]dr_2=0 \tag{44}$$

$$\frac{a}{h_1}\int_{-1}^{+1} G_1(r_1)dr_1=1, \quad \frac{b}{h_1}\int_{-1}^{+1} G_2(r_2)dr_2=1 \tag{45}$$

Due to the smooth contact at the endpoints a and b, the pressures $p_1(x)$ and $p_2(x)$ are zero at the edges. Consequently, Equation (38) has an index of -1, leading to the following expressions [38]:

$$G_1(r_{1i})=w_1(r_{1i})g_1(r_{1i}), \quad w_1(r_{1i})=\left(1-r_{1i}^2\right)^{1/2}, \quad (i=1,\ldots,N) \tag{46}$$

$$G_2(r_{2i})=w_2(r_{2i})g_2(r_{2i}), \quad w_2(r_{2i})=\left(1-r_{2i}^2\right)^{1/2}, \quad (i=1,\ldots,N) \tag{47}$$

where $g_1(r_1)$ and $g_2(r_2)$ are continuous and bounded functions within the interval $[-1,\ 1]$, respectively. Using Gauss–Chebyshev integration formulas [38,39], Equations (46)–(49) were transformed into a system of algebraic equations as follows:

$$\sum_{i=1}^{N} W_{1i} g_{1i}(r_{1i}) \left[\frac{a}{h_1} M_1(s_{1k}, r_{1i}) - \frac{\kappa_1 + 1}{8\, e^{\beta h_1}} \left(\frac{1}{r_1 - s_1} \right) \right] + \frac{b}{h_1} \sum_{i=1}^{N} W_{2i} g_{2i}(r_{2i}) M_2(s_{1k}, r_{2i}) = \frac{\pi}{2} \frac{\mu_0}{P/h_1} \frac{a/h_1}{R/h_1} s_{1k} \quad (k = 1, \ldots, N+1) \tag{48}$$

$$\frac{a}{h_1} \sum_{i=1}^{N} W_{1i} g_1(r_{1i}) N_1(s_{2k}, r_{1i}) + \sum_{i=1}^{N} W_{2i} g_2(r_{2i}) \left[\frac{b}{h_1} N_2(s_{2k}, r_{2i}) + \frac{\kappa_1 + 1}{4} \left(\frac{1}{r_2 - s_2} \right) + \frac{b}{h_1} L_1(s_{2k}, r_{2k}) \right] = 0 \quad (k = 1, \ldots, N+1) \tag{49}$$

$$\frac{a}{h_1} \sum_{i=1}^{N} W_{1i} g_1(r_{1i}) = 1, \quad \frac{b}{h_1} \sum_{i=1}^{N} W_{2i} g_2(r_{2i}) = 1 \tag{50}$$

where r_i and s_k are the zeros of the corresponding Chebyshev polynomials, and W_i^N is the weighting constant, given by the following expression:

$$W_i^N = \pi \left(\frac{1 - r_i^2}{N+1} \right), \quad (i = 1, \ldots, N) \tag{51}$$

$$r_i = \cos\left(\frac{i\pi}{N+1} \right), \quad (i = 1, \ldots, N) \tag{52}$$

$$s_k = \cos\left(\frac{\pi}{2} \frac{2k-1}{N+1} \right), \quad (k = 1, \ldots, N+1) \tag{53}$$

It can be shown that the $(N/2 + 1)$-th equations in (48) and (49) are automatically satisfied. As a result, Equations (48)–(50), together, provide a total of $2N + 2$ algebraic equations to solve for $2N + 2$ unknowns: $g_1(r_i)$ and $g_2(r_i)(i = 1, \ldots, N)$, along with the parameters a and b. The system is linear with respect to the functions $g_1(r_i)$ and $g_2(r_i)$, but it becomes nonlinear when solving for a and b. Therefore, an iterative approach is required to determine these two parameters.

3. Finite Element Modeling

Finite element modeling was employed to numerically validate the analytical formulation developed in this study. The contact system involving the functionally graded layer, homogeneous substrate, and Winkler foundation was implemented in ANSYS software [40]. The model's geometry, material properties, contact definitions, and boundary conditions were defined in accordance with the analytical configuration, and the obtained results were compared directly with the theoretical predictions.

The contact geometry used in the finite element analysis was assumed to be symmetric and half of the geometry was modeled and the analyses were performed. The FG layer's shear modulus was estimated using the grade function $\mu_1(y) = \mu_{0.e^{(\beta y)}}$. Since there is no function grading module in ANSYS, a new function was defined to vary the properties of the layers in the y direction. A finite element mesh with 28,099 quadrilateral solid elements, each with eight nodes, and 203 elements was used. The PLANE183 element has eight nodes, with each node having two degrees of freedom, including four corner nodes and four mid-nodes, with each node having two translational degrees of freedom in the x and y directions. Contact interaction between the FG layers, homogeneous layers, and rigid cylindrical stamp is also modeled in the simulation. Surface-to-surface contact was defined using CONTA169 and TARGE172 elements with the standard penalty-based contact algorithm available in ANSYS. The numerical solution was carried out using a nonlinear static analysis procedure with incremental load stepping to ensure stable convergence of the contact problem. The Winkler foundation is idealized with COMBIN 14, which is a linear spring element. A total of 4113 contact elements were added, in which the surfaces were represented with CONTA 169 and TARGE 172 in APDL. The finite element model of the contact problem used in the

study is shown in Figure 2. A mesh sensitivity check was performed to assess the adequacy of the selected discretization. Further mesh refinements resulted in negligible changes in the contact length and peak stress values, confirming that the adopted mesh density is sufficient for accurate contact analysis.

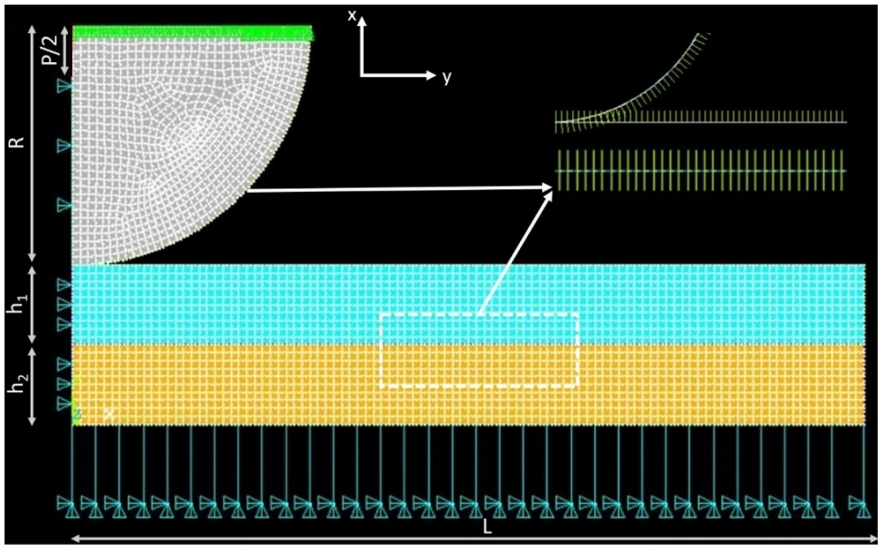


Figure 2. Finite element model of the problem.

The deformed geometry of the finite element model using different scales is shown in Figure 3. The FEM studies employed geometric dimensionless parameters such as cylindrical stamp radius (R/h_1), layer width (L/h_1), and layer height (h_1/h_2). In the analyses, the width and height of the layers were set at $L/h_1 = 50$ and $h_1/h_2 = 1$. On the other hand, other values required for the analyses were revised according to the desired analyses and the results were obtained.

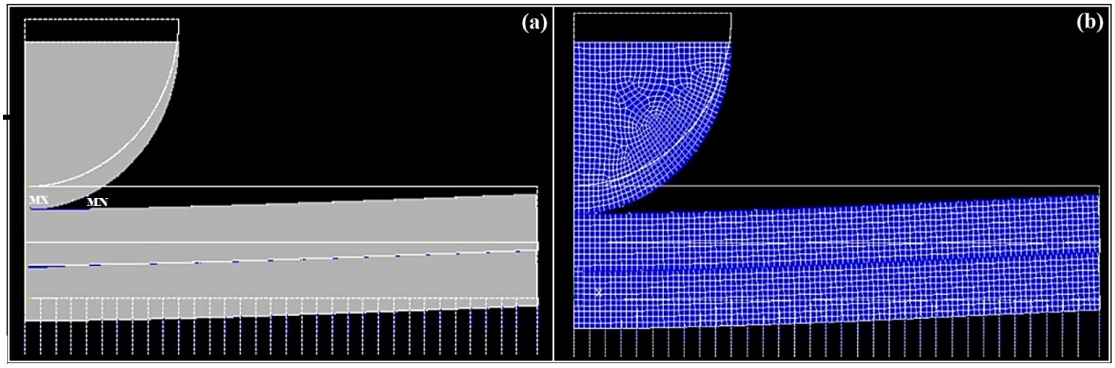


Figure 3. Deformed geometry of the contact model: (**a**) undeformed configuration without mesh visualization, (**b**) deformed configuration with finite element mesh.

Representative stress and displacement distributions obtained from the FEM simulations were also examined to verify that the predicted contact zones and stress gradients were consistent with the analytical solution.

4. Numerical Results

4.1. Contact Length

The contact length (a/h_1) between the rigid stamp and the FG layer for different stamp radius ratios ($R/h_1 = 10, 50, 100$) was calculated by both the analytical model, based on the theory of elasticity (ET), and the numerical model, based on FEMs, and the results are given in Table 1. As can be seen from the results, the contact distances increased with the

increase in the rigid stamp radius ratio. This behavior is mechanically consistent, since a larger stamp radius reduces local curvature and distributes the applied load over a wider region, leading to an expansion of the contact area. On the other hand, it is seen that the analytical solution results are quite compatible with that of the FEM solution, and a suitable FEM model is created in this context. More specifically, for all of the investigated stamp radius ratios and material gradation parameters, the relative error between the ET and FEM solutions remained within 1.25–2.18%, demonstrating strong quantitative agreement. The relative error (E%) is defined as $|\mathrm{ET} - \mathrm{FEM}|/\mathrm{ET} \times 100$.

Table 1. Comparison of the contact length (a/h1) between the rigid stamp and the FG layer with respect to the stamp radius ratio (R/h1), where (k = 1, $\mu_0/\mu_2 = 1$).

Parameter	R/h_1 = 10			R/h_1 = 50			R/h_1 = 100		
	ET	FEM	E(%)	ET	FEM	E(%)	ET	FEM	E(%)
$\beta_1 = -1$	0.151739	0.149	1.81	0.324858	0.320	1.50	0.450813	0.441	2.18
$\beta_1 = 0.01$	0.097590	0.096	1.63	0.221070	0.217	1.84	0.317386	0.312	1.70
$\beta_1 = 1$	0.061266	0.060	2.07	0.144055	0.141	2.12	0.212656	0.210	1.25

Table 2 shows the results for both the ET and the FEM with different stamp radius ratios (R/h_1 = 10, 50, 100) As can be seen, the contact distances increased as the stamp radius increased. From an interfacial mechanics perspective, the enlargement of the upper contact zone also influences the stress transfer toward the lower interface, resulting in a corresponding increase in b/h_1. In addition, it was determined by the analyses that the results of both analyses were quite consistent. The maximum deviation observed in Table 2 did not exceed 2.64%, confirming the robustness of the analytical formulation for interfacial contact length prediction.

Table 2. Comparison of the contact length (b/h_1) between the FG layer and the homogeneous layer as a function of the stamp radius ratio ($R/h1$), with (k = 1, $\mu_0/\mu_2 = 1$).

Parameter	R/h_1 = 10			R/h_1 = 50			R/h_1 = 100		
	ET	FEM	E (%)	ET	FEM	E (%)	ET	FEM	E (%)
$\beta_1 = -1$	1.336927	1.312	1.86	1.361852	1.331	2.27	1.390786	1.358	2.36
$\beta_1 = 0.01$	1.445485	1.426	1.35	1.455382	1.417	2.64	1.468406	1.450	1.25
$\beta_1 = 1$	1.598321	1.557	2.59	1.601851	1.570	1.99	1.606983	1.585	1.37

Table 3 shows the results for both the ET and the FEM for different elastic spring constant ratios. As can be seen, as the elastic spring constant ratio decreases, the system becomes more flexible and the contact distances also decrease. Physically, a softer foundation permits greater vertical deformation, reducing constraint at the interface and limiting the effective contact region. On the other hand, it was determined by the results that the elasticity theory solution (ET) and FEM obtained quite compatible results. Across all of the stiffness ratios, the discrepancy between the two methods remained below 3.28%, even for the most flexible foundation case, indicating stable numerical performance of the proposed model.

Table 3. Comparison of the contact length (a/$h1$) between the rigid stamp and the FG layer as a function of the elastic spring constant ratio ($k = k_0/\mu_2$), with ($R/h1 = 100$, $\mu_0/\mu_2 = 1$).

Parameter	k = 0.02			k = 0.1			k = 0.2		
	ET	FEM	E (%)	ET	FEM	E (%)	ET	FEM	E (%)
$\beta_1 = -1$	0.517983	0.510	1.54	0.477351	0.490	2.65	0.466473	0.480	2.90
$\beta_1 = 0.01$	0.362626	0.357	1.55	0.335652	0.344	2.49	0.328249	0.337	2.67
$\beta_1 = 1$	0.239327	0.236	1.39	0.223658	0.231	3.28	0.219241	0.222	1.26

Table 4 shows the results for both the ET and the FEM with different elastic spring constant ratios. As can be seen, the contact length increases significantly as the elastic spring constant ratio decreases. This trend reflects the redistribution of interface stresses due to foundation compliance, which alters the balance between local deformation and contact pressure transmission. It can also be seen from the table that the results of the two solutions are quite compatible with each other. The relative differences were generally within the range of 1.10–2.54%, reinforcing the predictive capability of the symmetry-based analytical solution.

Table 4. Comparison of the contact length (b/h_1) between the FG layer and the homogeneous layer as a function of the elastic spring constant ratio ($k = k_0/\mu_2$), with ($R/h1 = 100$, $\mu_0/\mu_2 = 1$).

Parameter	k = 0.02			k = 0.1			k = 0.2		
	ET	FEM	E (%)	ET	FEM	E (%)	ET	FEM	E (%)
$\beta_1 = -1$	3.095658	3.150	1.76	2.177473	2.218	1.86	1.856735	1.900	2.33
$\beta_1 = 0.01$	3.321718	3.401	2.39	2.342216	2.385	1.83	2.002576	2.050	2.37
$\beta_1 = 1$	3.618156	3.710	2.54	2.554162	2.613	2.30	2.194941	2.219	1.10

Table 5 shows the results for both the ET and the FEM for different shear modulus ratios ($R/h_1 = 10$, $k = 1$ constant). As can be seen, the contact length decreases significantly as the shear modulus ratio decreases. When the stiffness contrast between layers becomes more pronounced, load transfer becomes more localized near the interface, which narrows the contact region. It can also be seen from the table that consistent results are obtained between both solutions. For varying shear modulus contrasts up to $\mu_0/\mu_2 = 10$, the maximum deviation remained limited to 2.60%, demonstrating that the analytical model maintains accuracy even under strong material mismatch conditions.

Table 5. Comparison of the contact length (a/$h1$) between the rigid stamp and the FG layer as a function of the shear modulus ratio (μ_0/μ_2), with ($R/h1 = 10$, $k = 1$).

Parameter	μ_0/μ_2 = 1			μ_0/μ_2 = 2			μ_0/μ_2 = 10		
	ET	FEM	E (%)	ET	FEM	E (%)	ET	FEM	E (%)
$\beta_1 = -1$	0.151739	0.154	1.49	0.109098	0.108	1.01	0.049939	0.049	1.88
$\beta_1 = 0.01$	0.097590	0.099	1.44	0.068995	0.068	1.44	0.030802	0.030	2.60
$\beta_1 = 1$	0.061266	0.062	1.20	0.042878	0.042	2.05	0.018902	0.019	0.52

Table 6 shows the results for both the ET and the FEM for different shear modulus ratios ($R/h_1 = 10$, $k = 1$ constant). As can be seen, the contact length increased significantly as the shear modulus ratio increased. In this case, reduced stiffness mismatch allows stresses to spread more uniformly across the interface, resulting in an extended contact length. On the other hand, it was determined that very compatible results were obtained between the analytical and the numerical solutions, and the error rate remained below 3 for all cases. In particular, the highest deviation recorded in this set was 2.71%, while

most cases exhibited errors close to or below 2%, highlighting the reliability of the coupled analytical–numerical framework.

Table 6. Comparison of the contact length (b/$h1$) between the FG layer and the homogeneous layer as a function of the shear modulus ratio (μ_0/μ_2), with ($R/h1$ = 10, k = 1).

Parameter	μ_0/μ_2 = 1			μ_0/μ_2 = 2			μ_0/μ_2 = 10		
	ET	FEM	E (%)	ET	FEM	E (%)	ET	FEM	E (%)
$\beta_1 = -1$	1.336927	1.320	1.27	1.569336	1.545	1.55	2.305771	2.35	1.92
$\beta_1 = 0.01$	1.445485	1.420	1.76	1.726751	1.745	1.06	2.604380	2.65	1.75
$\beta_1 = 1$	1.598321	1.555	2.71	1.921335	1.945	1.23	2.944393	2.99	1.55

4.2. Contact Stress

Figure 4 shows the comparison of the contact stress distributions ($p_1(x)/P/h_1$) for different stamp radius ratios (R/h_1 = 10, 50, 100) with both the analytical and numerical models according to various β values. As can be seen, the stresses decrease as the stamp radii increase. The reason for this situation is the decrease in the stress per unit area, since the load is spread over a wider area. On the other hand, as can be seen from the figure, very compatible results were obtained from the ET solution and the FEM solution between the stresses. This shows that the created FEM model gives compatible results. Quantitatively, the peak stress values predicted by ET and FEM were nearly coincident, with differences visually negligible and consistent with the sub-3% deviations observed in the contact length calculations.

Figure 5 shows the contact stress between the FG layer and homogeneous layer with different stamp radii. As can be seen, as the rigid stamp diameter increases, the stress decreases, due to the load being spread over a wider area. On the other hand, it can be seen from the figure that very consistent results can be obtained with the ET and the FEM solutions.

Figure 6 shows the contact stress between the rigid stamp and FG layer with different elastic spring constant ratios. As can be seen from the figure, as the elastic spring constant ratio increases, the contact area will narrow, and the maximum stress values will increase slightly. On the other hand, it is seen that quite compatible results are obtained with ET and FEM.

Figure 7 shows the contact stress between FG layer and homogeneous layer with different elastic spring constant ratios. As can be seen, as the elastic spring constant ratio increases, the contact spreads to a narrower area and as a result, the maximum stresses increase. On the other hand, it is seen that ET and FEM are quite compatible in this analysis.

Figure 8 shows the contact stress between the rigid stamp and FG layer with different shear modulus ratios. As can be seen from the figure, as the shear modulus ratio increases, the maximum stress values increase significantly. The reason for this situation is that the upper layer becomes much more rigid than the lower layer and the load is concentrated in a narrower area. On the other hand, it can be clearly seen from the figure that the ET solution and the FEM solution for this analysis give very compatible results. Even under high shear modulus contrast (μ_0/μ_2 = 10), the stress distributions overlapped closely, confirming numerical stability under strong gradation effects.

Figure 9 shows the contact stress between FG layer and homogeneous layer with different shear modulus ratios. As can be seen from the figure, as the shear modulus ratio increases, that is, as the lower layer becomes more flexible than the upper layer, the maximum contact stresses decrease. The reason for this situation is that the load is spread over a wider area as the shear modulus increases. On the other hand, quite compatible results were obtained between the ET and FEM for all cases.

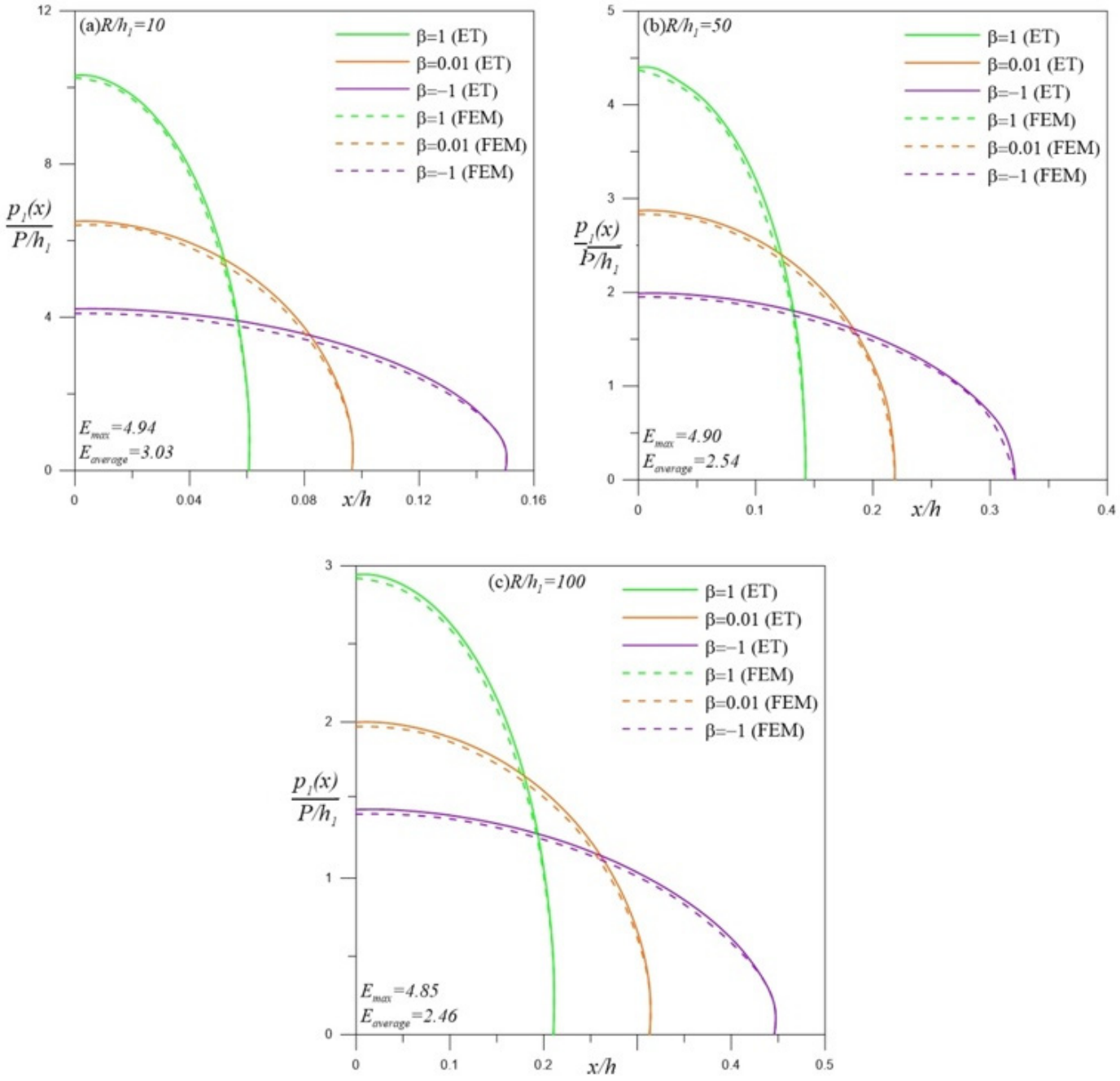


Figure 4. Contact stress between the rigid stamp and FG layer for different stamp radius ratios: (**a**) $R/h_1 = 10$, (**b**) $R/h_1 = 50$, (**c**) $R/h_1 = 100$ ($k = 1$, $\mu_0/\mu_2 = 1$).

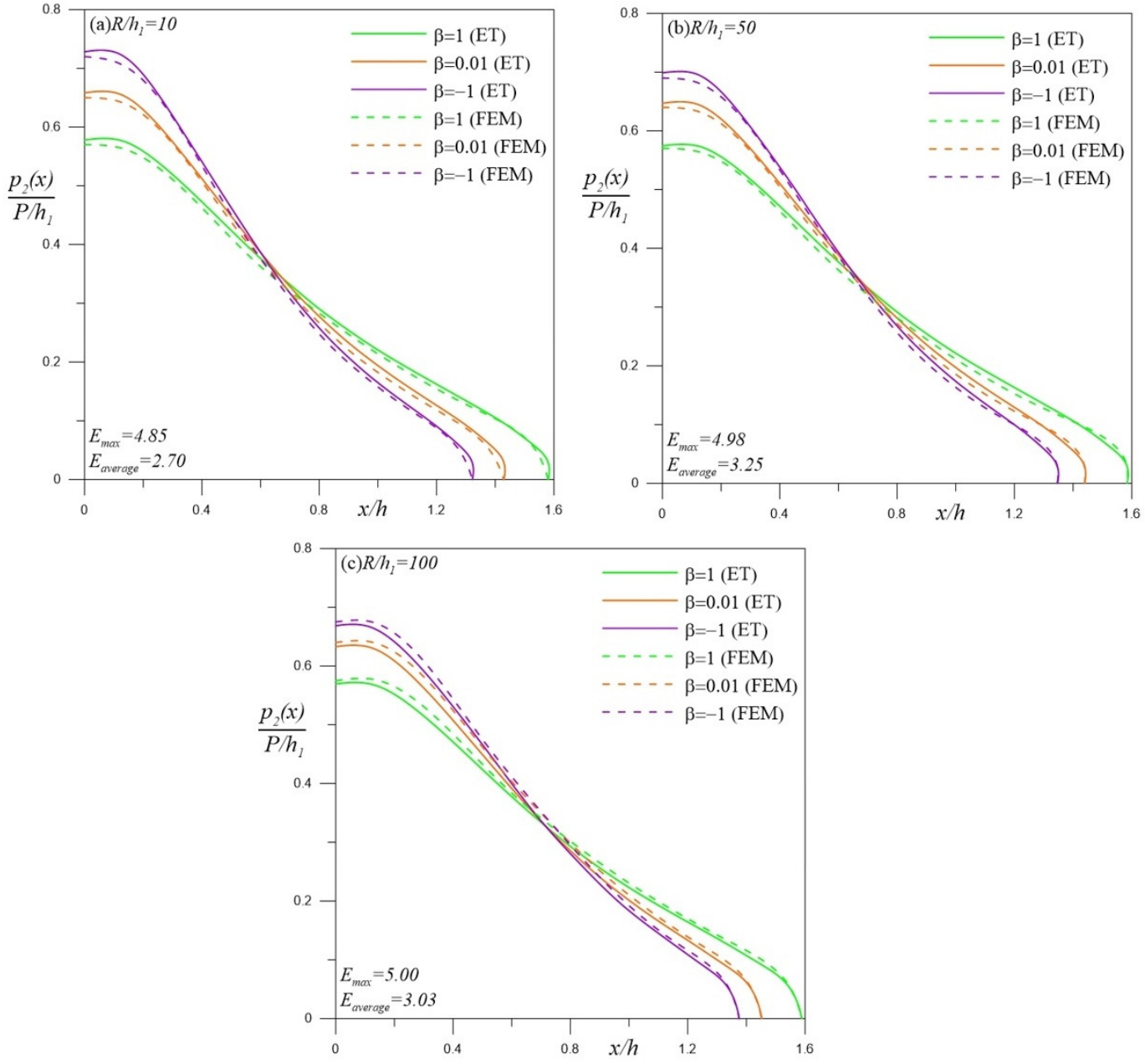


Figure 5. Contact stress between the FG layer and homogeneous layer with stamp radii: (**a**) $R/h_1 = 10$, (**b**) $R/h_1 = 50$, (**c**) $R/h_1 = 100$ ($k = 1$, $\mu_0/\mu_2 = 1$).

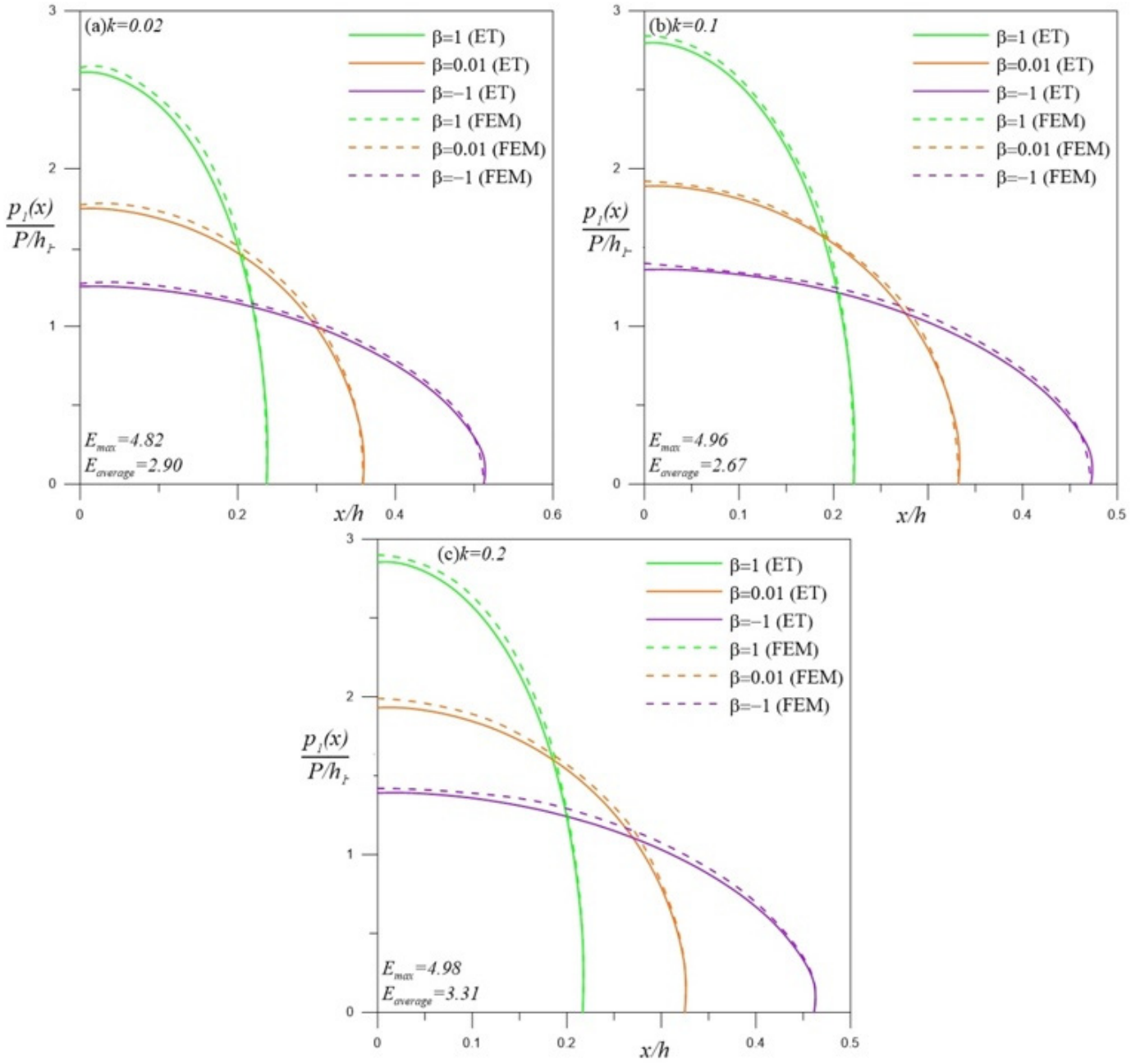


Figure 6. Contact stress between the rigid stamp and FG layer with elastic spring constant ratios: (**a**) k = 0.02, (**b**) k = 0.1, (**c**) k = 0.2.

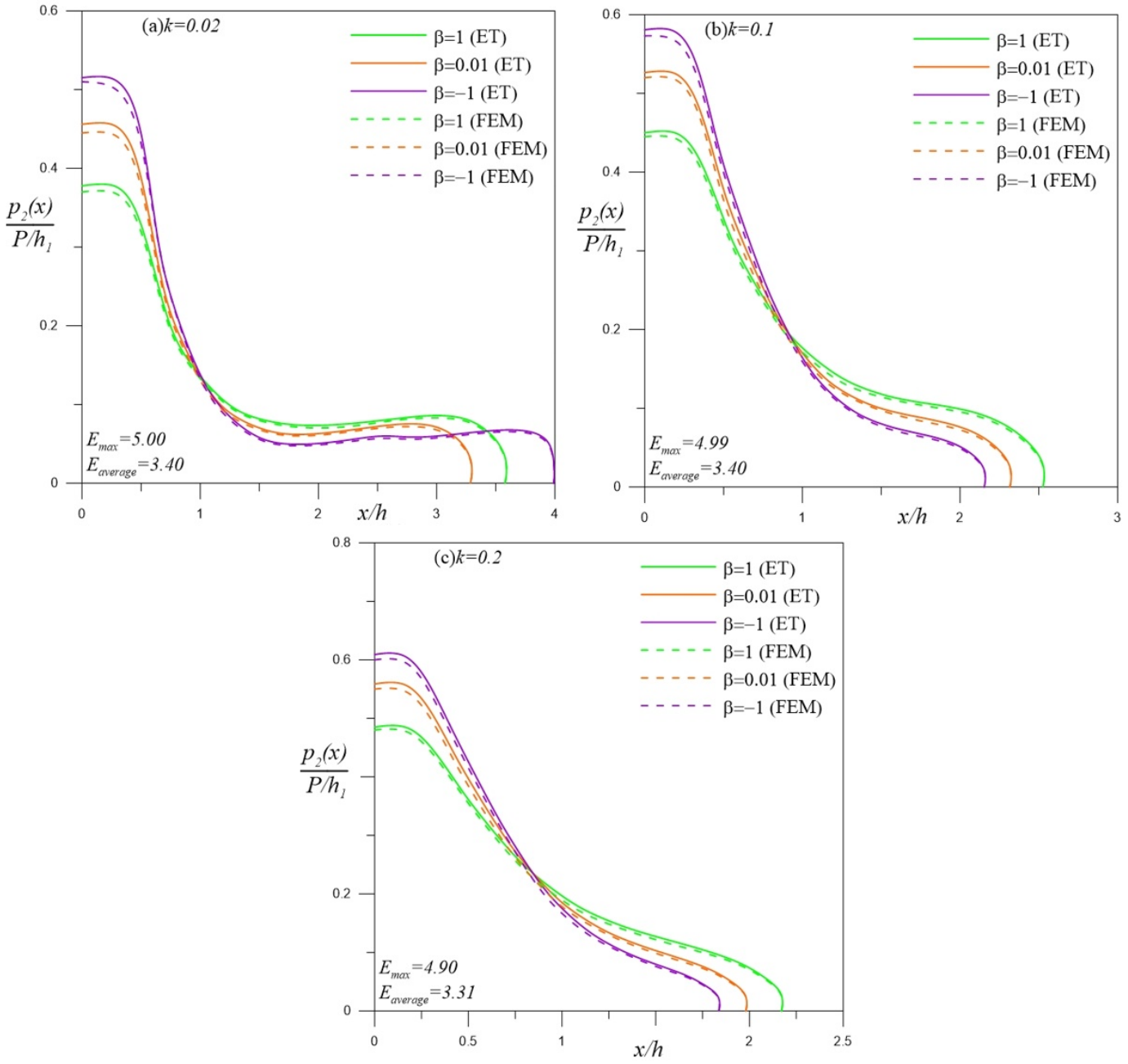


Figure 7. Contact stress between FG layer and homogeneous layer with elastic spring constant ratios: (**a**) k = 0.02, (**b**) k = 0.1, (**c**) k = 0.2.

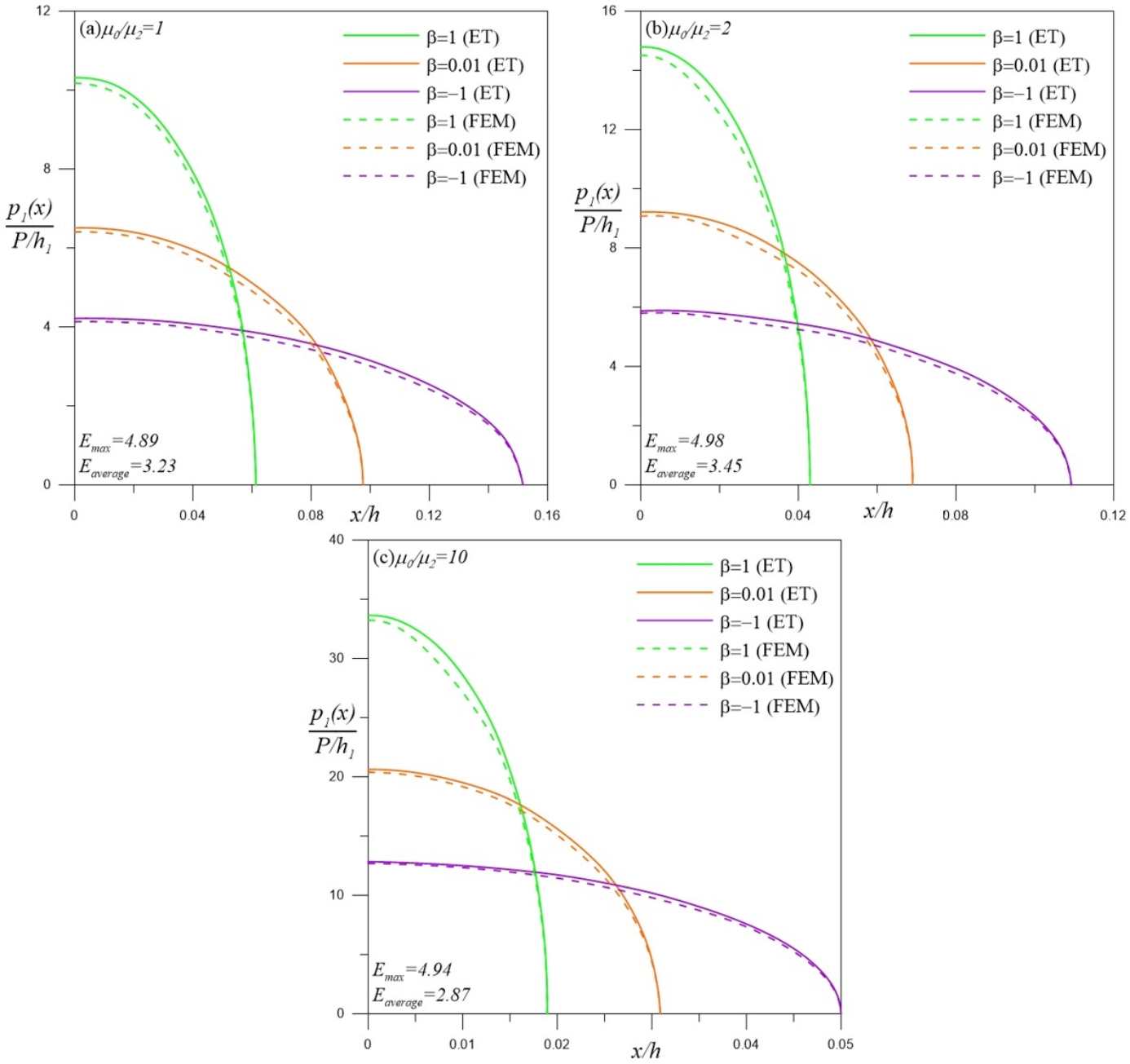


Figure 8. Contact stress between the rigid stamp and FG layer with shear modulus ratios: (**a**) $\mu_0/\mu_2 = 1$, (**b**) $\mu_0/\mu_2 = 2$ and (**c**) $\mu_0/\mu_2 = 10$.

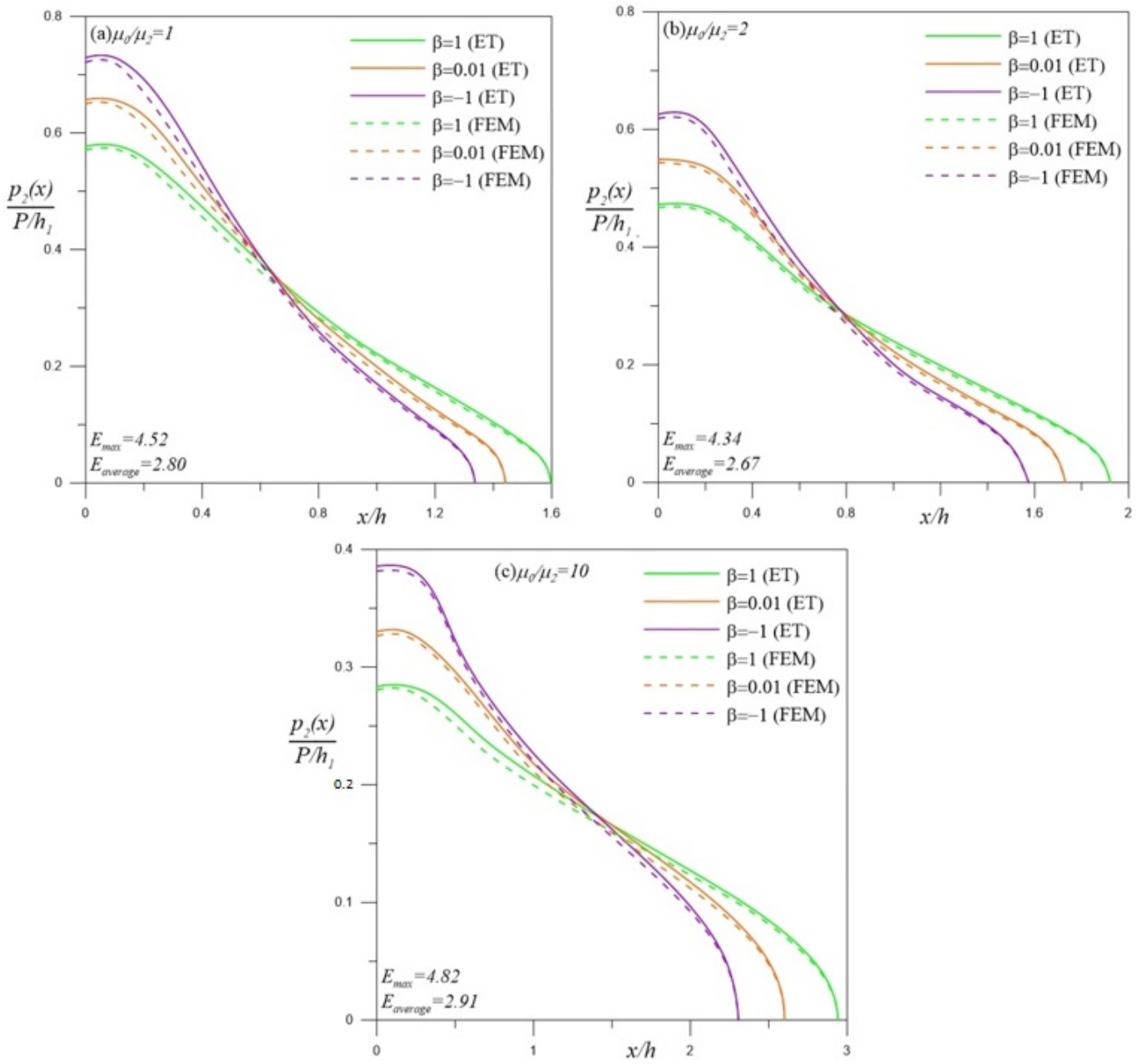


Figure 9. Contact stress between the FG and homogeneous layers with shear modulus ratios: (**a**) $\mu_0/\mu_2 = 1$, (**b**) $\mu_0/\mu_2 = 2$ and (**c**) $\mu_0/\mu_2 = 10$.

5. Significance and Contributions

This research offers many significant benefits in support of contact mechanics and material engineering. To begin with, the comparative validation process between the analytical model and numerical model improves the accuracy of the FEM in addressing complex contact problems with functionally graded layers and homogeneous layers. By examining the differences between these two models, it could be determined that there is substantial consistency in addressing contact problems via FEM simulation, which could be adopted for future work. Moreover, the outcomes obtained in this research have widespread applications in different fields of engineering, especially in the automobile, aerospace, and manufacturing sectors, where the performance of materials under the action of contact forces is critical. The applications described in this research apply to those systems in which materials are acted upon by pressure, friction, or contact forces, thereby being extremely useful for improved applications in these areas.

Another major benefit is its efficiency and flexibility in solving complex problems. It is faster compared to other traditional analysis techniques. Another major advantage is its appropriateness in solving problems involving complex geometries, which is not typical of other methods. It has particular importance in problems involving FGMs. These are materials whose properties vary in each direction in space, which cannot be solved in other ways. It is, therefore, appropriate in applications concerning those materials due to its efficiency, which is cost-effective. In addition, this study has made substantial contributions to improving the comprehension of contact stresses on FGMs from a mechanical point of view. It is anticipated that improved comprehension regarding deformation and stress responses in FGMs could lead to improved designs for these materials, resulting in their enhanced functionality in high-pressure contacts, among other difficult conditions. The findings of this study provide a basis for improving the performance and functionality of FGM-based designs in aviation, automotive, and energy applications.

Finally, with the combination of theoretical concepts and computational analysis, there is comprehensiveness in addressing receding contact problems in this research work. By incorporating the theory of elasticity with computational simulations in FEM, there is scope for advancing in a strengthened manner to analyze contacts in multi-layered media, which could lead to further investigation in contacts with more complex conditions, for example, dynamic loading problems, in the future. The introduction of optimization concepts could also be explored for advancing designs related to FGMs.

6. Relevance to Aerospace Engineering and Symmetry/Asymmetry Considerations

The functionally graded and multi-layered elastic media studied in this work are directly applicable to many space and aviation applications where parts are subjected to strongly localized loads and severe environmental gradients [41]. In space vehicle structural design, FGMs are becoming increasingly prominent in thermal protection layers, propulsion subsystems, and adaptive structural panels where structural or thermomechanical response patterns are strongly dependent on the stress transmission patterns at the interfaces between graded and homogeneous layers. The nonlinear parameter-dependent contact problem studied in this work can provide important guidance on how materials in space vehicles react to strongly localized loading during launch entry, atmospheric re-entry, and in-orbit procedures [42].

From a symmetry perspective, many aerospace contact configurations such as cylindrical landing pads, docking interfaces, and axis-aligned structural supports exhibit geometric and loading symmetry. The analytical formulation developed in this study explicitly exploits this symmetry to reduce the problem domain and obtain tractable integral equations, while still capturing essential contact mechanics behavior relevant to these applications. Therefore, the symmetry-based approach is not only mathematical but also consistent with typical aerospace interface configurations.

One crucial usage is seen in planetary touchdowns, where either the footpads on landers or wheels on rovers are in contact with stratified media featuring loose regolith on top of compact bottom layers. This stratified planetary soil has similarities to the graded and homogeneous-contacting body problem examined above, in that either the actual or perceived interface areas either expand or contract, depending on various soil properties and geometry [43]. This nonlinear load-dependent evolution of the interface boundaries can provide insight into how actual touchdowns are accomplished on stratified planetary soils. It remains very important for forthcoming missions to both the Moon and Mars, as well as for asteroids. Apart from landing mechanisms, other areas where the implications of this work are applicable include soft-contact mechanisms for space robots and space

docking. Capture mechanisms, space robots' end-effectors, and soft-contact grippers often encounter complex spacecraft surfaces where the contact region varies depending on the applied force. The force transfer and stress sensitivity to stiffness contrast and gradient parameters demonstrated in this work are also applicable to space robots, where controlling force transfer is important for operational safety [38]. In general, FGMs are emerging as promising materials for advanced spacecraft design, including heat-protection coatings, protection layers against micro-meteroids, piezo-composites for actuations, and bonding layers in deployable spacecraft structures [44,45]. The FEM framework for analysis and the validated results described in this article can serve as a basis for predicting the behavior of various systems subjected to heavy mechanical loads. Nonlinear and gradient-driven processes typical of layered contacts are applied in various ways in this work for improving design efficiency in space missions subjected to severe operating conditions.

7. Conclusions

In this study, the receding contact behavior of a functionally graded bi-layer system resting on an elastic foundation was investigated using an analytical formulation and finite element modeling. The primary scientific contribution of this work lies in the development and validation of a symmetry-based analytical formulation for a graded homogeneous layered system with evolving contact boundaries, supported by a systematic parametric analysis. The main findings of this study can be summarized as follows:

- The analytical formulation based on elasticity theory showed strong agreement with the FEM results, with relative differences generally remaining below 3.3% for contact length predictions across all investigated parameter combinations.
- Increasing the stamp radius ratio (R/h_1 = 10–100) led to a significant increase in the contact length at both interfaces. For the examined cases, relative deviations between ET and FEM remained within 1.25–2.64%, confirming the robustness of the analytical model.
- Decreasing the elastic spring constant ratio (k = 0.02–0.2) increased the structural compliance of the system, modifying the contact length and stress distribution. Even for the most flexible foundation case, discrepancies between ET and FEM did not exceed 3.28%.
- Variations in the shear modulus ratio (μ_0/μ_2 = 1–10) significantly influenced contact behavior. Increasing the stiffness contrast resulted in reduced contact length and more localized stress transfer. The maximum deviation between analytical and numerical predictions remained below 2.71% in all examined cases.
- The coupled analytical and finite element framework provides a consistent and reliable approach for predicting receding contact behavior in layered graded structures subjected to localized mechanical loading.
- The obtained results are directly relevant to layered aerospace systems, including landing pads interacting with stratified media, protection layers under concentrated loading, and contact interfaces in controlled force transmission mechanisms.

These findings may assist in preliminary design assessments of graded aerospace components by providing quantitative estimates of contact length evolution under varying stiffness contrasts and geometric parameters. The presented framework can therefore support material gradation selection and interface design in layered structural systems subjected to localized loading.

The overall trends obtained in this study are consistent with previously reported analytical and numerical investigations of receding contact in layered and graded systems. Minor quantitative differences may arise from the specific exponential material gradation and the adopted foundation modeling approach. In this respect, the present results both

confirm and extend the general understanding of stiffness- and geometry-dependent contact behavior.

The present analytical model is developed within the framework of linear elasticity and small deformation theory under frictionless contact assumptions. Therefore, its applicability is limited to cases where geometric nonlinearities and tangential interface effects are negligible. Extension of the formulation to include large deformation behavior or frictional contact conditions would require nonlinear constitutive modeling and additional boundary constraints, which may be considered in future studies.

Author Contributions: A.A.: Writing—original draft, Investigation; M.T.: Writing—original draft, Software, Investigation; A.E.: Writing—original draft, Methodology, Data curation; M.Y.: Review and editing, Software, Project administration, Visualization; D.M.S.: Writing—review and editing, Formal analysis, Visualization; S.N.: Writing—original draft, Validation; E.U.Y.: Writing—review and editing, Investigation, Resources; D.A.D.: Review and editing, Software; A.B.: Conceptualization, Methodology, Supervision. All authors have read and agreed to the published version of the manuscript.

Funding: This research received no external funding.

Data Availability Statement: The data presented in this study are available on request from the corresponding author.

Conflicts of Interest: The authors declare no conflicts of interest.

Appendix A

$$\begin{aligned}\Delta_1 = \mu_1\Big(&e^{h_1(m_1+n_2)}(C_1C_3D_2D_4 - C_1C_4D_2D_3 - C_2C_3D_1D_4 + C_2C_4D_1D_3)\\ &+e^{h_1(n_1+n_3)}(-C_1C_2D_3D_4 + C_1C_4D_2D_3 + C_2C_3D_1D_4 - C_3C_4D_1D_2)\\ &+e^{h_1(m_1+n_4)}(C_1C_2D_3D_4 - C_1C_3D_2D_4 - C_2C_4D_1D_3 + C_3C_4D_1D_2)\\ &+e^{h_1(n_2+n_3)}(C_1C_2D_3D_4 - C_1C_3D_2D_4 - C_2C_4D_1D_3 + C_3C_4D_1D_2)\\ &+e^{h_1(n_2+n_4)}(-C_1C_2D_3D_4 + C_1C_4D_2D_3 + C_2C_3D_1D_4 - C_3C_4D_1D_2)\\ &+e^{h_1(n_3+n_4)}(C_1C_3D_2D_4 - C_1C_4D_2D_3 - C_2C_3D_1D_4 + C_2C_4D_1D_3)\Big)\end{aligned} \tag{A1}$$

$$\begin{aligned}\Delta_2 = &4\xi - k - \kappa_2 k - 8\xi e^{2\xi h_2} + 4\xi e^{4\xi h_2} + ke^{4\xi h_2}\\ &-16\xi^3 {h_2}^2 e^{2\xi h_2} + \kappa_2 k e^{4\xi h_2} + 4\xi h_2 k e^{2\xi h_2} + 4\kappa_2 \xi h_2 k e^{2\xi h_2}\end{aligned} \tag{A2}$$

Appendix B

$$n_1 = -\frac{1}{2}\left(\beta + \sqrt{4\xi^2 + \beta^2 - 4\xi\beta i\sqrt{\frac{3-\kappa_1}{\kappa_1+1}}}\right)$$

$$n_2 = -\frac{1}{2}\left(\beta - \sqrt{4\xi^2 + \beta^2 - 4\xi\beta i\sqrt{\frac{3-\kappa_1}{\kappa_1+1}}}\right)$$

$$n_3 = -\frac{1}{2}\left(\beta + \sqrt{4\xi^2 + \beta^2 + 4\xi\beta i\sqrt{\frac{3-\kappa_1}{\kappa_1+1}}}\right)$$

Appendix C

$$M_1(x_1,t_1)=\int_0^{\infty}\left[\frac{\xi}{2\Delta_1}\left(\sum_{j=1}^{4}A_{j1}m_j e^{n_j h_1}\right)+\frac{\kappa_1+1}{8}\frac{1}{\mu_0 e^{\beta h_1}}\right]\sin(\xi(t_1-x_1))d\xi \tag{A3}$$

$$M_2(x_1,t_2)=\int_0^{\infty}\left(\frac{\xi}{2\Delta_1}\sum_{j=1}^{4}A_{j2}m_j e^{n_j h_1}\right)\sin(\xi(t_2-x_1))d\xi \tag{A4}$$

$$N_1(x_2,t_1)=\int_0^{\infty}\frac{\xi}{2\mu_0 e^{\beta h_1}\Delta_1}\sum_{j=1}^{4}A_{j1}m_j\sin(\xi(t_1-x_2))d\xi \tag{A5}$$

$$N_2(x_2,t_2)=\int_0^{\infty}\left[\frac{\xi}{2\mu_0\Delta_1}\sum_{j=1}^{4}A_j m_{j2}-\frac{\kappa_1+1}{4\mu_1}\right]\sin(\xi(t_2-x_2))d\xi \tag{A6}$$

$$\begin{aligned}L_1(x_2,t_2)=\int_0^{\infty}\frac{1}{8\mu_2\Delta_2}\Big\{&-4\xi+k-4\kappa_2\xi+2\kappa_2 k+\kappa_2^2 k+4\kappa_2\xi e^{4\xi h_2}-4\kappa_2 k e^{2\xi h_2}+2\kappa_2 k e^{4\xi h_2}+\\&16\kappa_2\xi^2 h_2 e^{2\xi h_2}-2\kappa_2^2 k e^{2\xi h_2}+\kappa_2^2 k e^{4\xi h_2}-2k e^{2\xi h_2}+k e^{4\xi h_2}+4\xi e^{4\xi h_2}+16\xi^2 h_2 e^{2\xi h_2}\Big\}\sin(\xi(t_2-x_2))d\xi\end{aligned} \tag{A7}$$

References

1. Ma, X.; An, N.; Cong, Q.; Bai, J.-B.; Wu, M.; Xu, Y.; Zhou, J.; Zhang, D.; Zhang, T.; Guo, R. Design, modeling, and manufacturing of high strain composites for space deployable structures. *Commun. Eng.* **2024**, *3*, 78. [CrossRef]
2. Vlazakis, P. *Modular Re-Design of a Micro-Launcher Component*; Luleå University of Technology: Luleå, Sweden, 2024.
3. Bayar, B. Designing Extraterrestrial Habitats on Mars and the Moon: An Overview of Environmental Conditions and Design Considerations. In *International Civil Engineering and Architecture Conference*; Springer: Berlin/Heidelberg, Germany, 2024.
4. Kalapodis, N.; Kampas, G.; Ktenidou, O.-J. A review towards the design of extraterrestrial structures: From regolith to human outposts. *Acta Astronaut.* **2020**, *175*, 540–569. [CrossRef]
5. Li, B.; Hang, Z.; Dai, T. Thermomechanical Behaviors of a Novel Double-Layer Corrugated Core Structure for Thermal Protection System. *Int. J. Aerosp. Eng.* **2023**, *2023*, 5315977. [CrossRef]
6. Xu, Q.; Li, S.; Meng, Y. Optimization and re-design of integrated thermal protection systems considering thermo-mechanical performance. *Appl. Sci.* **2021**, *11*, 6916. [CrossRef]
7. Deierling, P.; Zhupanska, O.I.; Pasiliao, C.L. Thermo-mechanical behavior of spatially tailored functionally graded materials in a high temperature environment. In *Proceedings of the American Society for Composites: Thirtieth Technical Conference*; IOWA: Iowa City, IA, USA, 2015; pp. 1462–1472.
8. Cao, C.; Ali, A.B.; Hussein, Z.A.; Singh, N.S.S.; Abdullaeva, B.; Zubair, A.; Salahshour, S.; Baghaei, S. Analysis of different phase change materials (PCMs) and wall material in a nano-circular space thermal energy storage (TES) system: A molecular dynamics approach. *Int. J. Therm. Sci.* **2025**, *215*, 109954. [CrossRef]
9. Tao, H.; Aldlemy, M.S.; Homod, R.Z.; Aksoy, M.; Mohammed, M.K.; Alawi, O.A.; Togun, H.; Goliatt, L.; Khan, M.M.H.; Yaseen, Z.M. Hybrid nanocomposites impact on heat transfer efficiency and pressure drop in turbulent flow systems: Application of numerical and machine learning insights. *Sci. Rep.* **2024**, *14*, 19882. [CrossRef]
10. Pan, Z.; Cheng, J.; Zhao, L.; Ragab, A.E. Thermo-dynamic response of multi-directional functionally graded panels resting on an elastic substrate with the aid of data-driven solution. *Aerosp. Sci. Technol.* **2023**, *143*, 108724. [CrossRef]
11. Besisa, D.; Ewais, E. Advances in functionally graded materials and structures. In *Advances in Functionally Graded Ceramics—Processing, Sintering Properties and Applications*; InTech: London, UK, 2016; Volume 1, pp. 1–31.
12. Feng, X.; Liu, W.; Liu, C. Thermal-mechanical coupling analysis of functionally graded cylindrical shells. *IOP Conf. Ser. Mater. Sci. Eng.* **2019**, *576*, 012006. [CrossRef]
13. Mishra, P.; Gupta, V.; Malwe, P.D.; Urade, A.; Khanke, V.; Siddiqui, M.I.H.; Dixit, S.; Chan, C.K.; Sonawane, C.; Tejani, G.G. Ratcheting fatigue behaviour of advanced structural materials at their service temperatures. *Sci. Rep.* **2025**, *15*, 28115. [CrossRef] [PubMed]
14. Forsbach, F.; Heß, M. Shear-off behavior of adhesive contacts with functionally graded elastic media. *J. Adhes.* **2025**, *101*, 1516–1541. [CrossRef]
15. Han, L.F.; Liu, T.J. Sliding frictional and adhesive coupling contact analysis of FGPM layered half-space under an insulating indenter. *Int. J. Solids Struct.* **2024**, *299*, 112874. [CrossRef]

16. Tian, X.; Zhou, Y.; Ding, S.; Wang, L. Exploring the effects of finite size and indenter shape on the contact behavior of functionally graded thermoelectric materials. *Int. J. Solids Struct.* **2024**, *305*, 113089. [CrossRef]
17. Tian, X.; Zhou, Y.; Zhang, C. On the imperfect interface of a functionally graded thermoelectric layered structure. *Compos. Struct.* **2023**, *322*, 117394. [CrossRef]
18. Karabulut, P.M.; Çetinkaya, I.T.; Oğuz, H.; Çömez, İ. Moving contact problem of a functionally graded orthotropic coated half plane. *Acta Mech.* **2024**, *235*, 3989–4004. [CrossRef]
19. Adıyaman, G.; Birinci, A.; Öner, E.; Yaylacı, M. A receding contact problem between a functionally graded layer and two homogeneous quarter planes. *Acta Mech.* **2016**, *227*, 1753–1766. [CrossRef]
20. Yaylacı, M.; Eyüboğlu, A.; Adıyaman, G.; Yaylacı, E.U.; Öner, E.; Birinci, A. Assessment of different solution methods for receding contact problems in functionally graded layered mediums. *Mech. Mater.* **2021**, *154*, 103730. [CrossRef]
21. Yaylacı, M.; Birinci, A. The receding contact problem of two elastic layers supported by two elastic quarter planes. *Struct. Eng. Mech. Int'l J.* **2013**, *48*, 241–255. [CrossRef]
22. Yaylacı, M.; Yaylı, M.; Öztürk, Ş.; Ay, S.; Özdemir, M.E.; Yaylacı, E.U.; Birinci, A. Examining the contact problem of a functionally graded layer supported by an elastic half-plane with the analytical and numerical methods. *Math. Methods Appl. Sci.* **2024**, *47*, 10400–10420. [CrossRef]
23. Yaylacı, M.; Öner, E.; Adıyaman, G.; Öztürk, Ş.; Uzun Yaylacı, E.; Birinci, A. Analyzing of continuous and discontinuous contact problems of a functionally graded layer: Theory of elasticity and finite element method. *Mech. Based Des. Struct. Mach.* **2024**, *52*, 5720–5738. [CrossRef]
24. Yan, J.; Wang, C. Receding contact problem of multi-layered elastic structures involving functionally graded materials. *Crystals* **2022**, *12*, 354. [CrossRef]
25. Asiri, S.A.; Akbaş, Ş.D.; Eltaher, M.A. Damped dynamic responses of a layered functionally graded thick beam under a pulse load. *Struct. Eng. Mech. Int'l J.* **2020**, *75*, 713–722.
26. Wang, C.; Ping, X.; Wang, X. An adaptive finite element method for crack propagation based on a multifunctional super singular element. *Int. J. Mech. Sci.* **2023**, *247*, 108191. [CrossRef]
27. Aktarer, S.M.; Kucukomeroglu, T.; Sekban, D.M.; Yaylaci, E.U.; Yaylaci, M.; Ozdemir, M.E.; Mirzaloglu, I. Analysis of the changes in microstructure, mechanical, and contact properties of multi-pass friction stir processed DP800 steel. *Adv. Nano Res.* **2025**, *18*, 253–264.
28. Yan, J.; Mi, C. A receding contact analysis for an elastic layer reinforced with a functionally graded coating and pressed against a half-plane. *J. Mech. Sci. Technol.* **2019**, *33*, 4331–4344. [CrossRef]
29. Lin, W. Stress analysis of thick-Wall hollow functionally graded material based on plane strain problem. *J. Phys. Conf. Ser.* **2021**, *1838*, 012006. [CrossRef]
30. Chidlow, S.; Teodorescu, M.; Vaughan, N.D. A solution method for the sub-surface stresses and local deflection of a semi-infinite inhomogeneous elastic medium. *Appl. Math. Model.* **2012**, *36*, 3486–3501. [CrossRef]
31. Wang, Q.J.; Sun, L.; Zhang, X.; Liu, S.; Zhu, D. FFT-based methods for computational contact mechanics. *Front. Mech. Eng.* **2020**, *6*, 61. [CrossRef]
32. Jagota, V.; Sethi, A.P.S.; Kumar, K. Finite element method: An overview. *Walailak J. Sci. Technol.* **2013**, *10*, 1–8.
33. Liu, S.; Fang, G.; Fu, M.; Yan, X.; Meng, S.; Liang, J. A coupling model of element-based peridynamics and finite element method for elastic-plastic deformation and fracture analysis. *Int. J. Mech. Sci.* **2022**, *220*, 107170. [CrossRef]
34. Cherif, A.A.; Abdelmadjid, M.; El Sallah, Z.M.; Ali, B.; Yaylacı, M.; Abderahmane, S.; Özdemir, M.E.; Dizdar, A.; Yaylacı, E.U.; Güvercin, Y. Comparative study by FEM of different liners of a transfemoral amputated lower limb. *Sci. Rep.* **2025**, *15*, 31878. [CrossRef] [PubMed]
35. Sekban, D.M.; Yaylaci, E.U.; Ozdemir, M.E.; Yaylaci, M. Determination of formability behavior of steel used in ships by various methods. *Struct. Eng. Mech. Int. J.* **2024**, *92*, 189–196.
36. Sekban, D.M.; Olmez, H. Effect of stress-strain curve changing with equal channel angular pressing on ultimate strength of ship hull stiffened panels. *Struct. Eng. Mech. Int. J.* **2021**, *78*, 473–484.
37. Chen, X.; Liu, Y. *Finite Element Modeling and Simulation with ANSYS Workbench*; CRC Press: Boca Raton, FL, USA, 2018.
38. Erdogan, F.; Gupta, G.D. On the numerical solution of singular integral equations. *Q. Appl. Math.* **1972**, *29*, 525–534. [CrossRef]
39. Jen, E.; Jen, E.; Srivastav, R.P. Solving singular integral equations using Gaussian quadrature and overdetermined systems. *Comput. Math. Appl.* **1983**, *9*, 625–632. [CrossRef]
40. Kaya, F.; Polat, A. Stress analysis of the contact problem in a functionally graded layer loaded with a distributed load and two rigid circular punches resting on an elastic two quarter planes. *Forces Mech.* **2023**, *11*, 100203. [CrossRef]
41. Miteva, A.; Bouzekova-Penkova, A. Some aerospace applications of functionally graded materials. *Aerosp. Res. Bulg.* **2021**, *33*, 195–209.
42. Liaoliang, K.; Yuesheng, W. Progress in some basic problems on contact mechanics of functionally graded materials. *Chin. Sci. Bull.* **2015**, *60*, 1565–1573. [CrossRef]

43. Li, Y.; Feng, Z.; Hao, L.; Huang, L.; Xin, C.; Wang, Y.; Bilotti, E.; Essa, K.; Zhang, H.; Li, Z. A review on functionally graded materials and structures via additive manufacturing: From multi-scale design to versatile functional properties. *Adv. Mater. Technol.* **2020**, *5*, 1900981. [CrossRef]
44. Min, L.; Liu, Q.; Liu, L. Crack growth simulation of functionally graded materials based on improved bond-based peridynamic model. *Materials* **2021**, *14*, 3032. [CrossRef] [PubMed]
45. Noda, N.; Nakai, S.; Tsuji, T. Thermal stresses in functionally graded material of particle-reinforced composite. *JSME Int. J. Ser. A Solid Mech. Mater. Eng.* **1998**, *41*, 178–184.

Disclaimer/Publisher's Note: The statements, opinions and data contained in all publications are solely those of the individual author(s) and contributor(s) and not of MDPI and/or the editor(s). MDPI and/or the editor(s) disclaim responsibility for any injury to people or property resulting from any ideas, methods, instructions or products referred to in the content.